Influence of the dry aerosol particle size distribution and morphology on the cloud condensation nuclei activation. An experimental and theoretical investigation

Junteng Wu[1], Alessandro Faccinetto[1], Symphorien Grimonprez[1], Sébastien Batut[1], Jérôme Yon[2], Pascale Desgroux[1], Denis Petitprez[1]

[1]Lille Univ., CNRS PC2A, 59000 Lille, France
[2]Normandie Univ., INSA Rouen, UNIROUEN, CNRS CORIA, 76000 Rouen, France

Correspondence to: Alessandro Faccinetto (alessandro.faccinetto@univ-lille.fr)

Abstract. The modern parametrization of the classical theory of nucleation (κ-Köhler theory) implicitly assumes a Dirac delta distribution to model the density of ideal spherical point size dry particles and droplets. However, anthropogenic activities like combustion or other high temperature processes frequently result in the emission of aerosols in the form of polydisperse fractal-like aggregates composed of condensed phase nanoparticles (for instance soot). If certain conditions are met, the emitted particles are known to evolve into important cloud condensation nuclei (CCN) in the atmosphere, however their behavior as CCN can deviate significantly from theoretical predictions. In this work, an extension of κ-Köhler theory is proposed that takes into account the effect of the size distribution and particle morphology on the activation of the aerosol dry particles. A theoretical and experimental approach are combined to derive the dependence of the activated fraction on supersaturation $F_a = F_a(SS)$ on parameters that describe the size distribution and morphology of the particles like the geometric standard deviation and the fractal dimension of the aggregates. The model is tested on two different aerosols, a simple case of isolated quasi-spherical ammonium sulfate particles generated by atomization, and complex morphology soot aggregates generated by a laboratory diffusion jet flame.

Keywords. κ-Köhler theory, cloud condensation nuclei (CCN), size distribution, morphology, ammonium sulfate, soot.

1. Introduction

To the present day, Köhler theory is widely used to describe the formation process of liquid cloud droplets and to understand the role of atmospheric aerosols as cloud condensation nuclei (CCN). The classical Köhler theory (Köhler, 1936) is entirely founded on equilibrium thermodynamics, and describes the change of the saturation

5   vapor pressure of water induced by the curved surface of the nascent droplet and by the presence of solutes in the liquid phase. The internally mixed nature of many atmospheric aerosols is accounted for in a more modern approach, the so-called κ-Köhler theory (Petters and Kreidenweis, 2007), that combines the classical theory and a single parameter (κ) representation of the CCN activity to gain access to a variety of partially soluble components. However, neither the classical nor the κ-Köhler theory account for the dry aerosol particle size

10   distribution and morphology. For all practical purposes, both theories operate under the hypothesis of Dirac delta distributions of spherical dry particles and droplets, and implicitly consider the volume equivalent diameter d_{ve} as representative of the size of the aerosol particles. Many successful applications of the κ-Köhler theory on mineral dust, marine aerosols, inorganic water-soluble aerosols and secondary organic aerosols exist in the literature (Farmer et al., 2015; Fofie et al., 2018; Tang et al., 2015, 2016). However, the κ-Köhler theory is less

15   effective when applied to atmospheric aerosols characterized by large geometric deviation or complex morphology, and more specifically, the crossing of the Kelvin limit has been reported in several instances (Lambe et al., 2015; Tritscher et al., 2011).

Herein, a theoretical approach is proposed to include the contribution of the size distribution and morphology of the dry particles into κ-Köhler theory for aerosols of atmospheric interest, which aims to make quantitative

20   predictions on the activated fraction as a function of the supersaturation $F_a = F_a(SS)$ during the aerosol activation process. To test the model, activation experiments are performed in water supersaturation conditions using two different aerosols as CCNs. The first aerosol is a close-to-ideal case of size-selected, isolated spherical particles (ammonium sulfate nanoparticles dispersed in nitrogen), while the second aerosol is a more complex case of polydisperse fractal-like aggregates (soot activated by exposure to ozone) that represents realistic anthropogenic

25   emissions in the atmosphere.

2. Theory

2.1. Classical and κ-Köhler theory

According to Köhler theory, the supersaturation $SS(D)$ over an aqueous solution droplet as a function of the droplet diameter D is given by:

$$SS(D) = \frac{p_{w,D}^*}{p_{w,\infty}^*} = a_w \exp\left(\frac{A}{D}\right) - 1, \qquad A = \frac{4 M_w \sigma_{s/a}}{R\, T\, \rho_w} \qquad \text{Eq. (1)}$$

30   where $p_{w,D}^*$ is the equilibrium vapor pressure over a curved surface, p_w^* is the equilibrium vapor pressure over a flat water surface ($p_{w,\infty}^* = p_w^*$), a_w, M_w and ρ_w are the chemical activity, molar mass and density of water, respectively, $\sigma_{s/a}$ is the surface tension at the solution/air interface, R is the ideal gas constant and T is the

temperature. $\sigma_{s/a} = 0.072$ J m^{-2} and $T = 298$ K are commonly used for calculations that lead to $A \simeq 2.09$ nm. For the sake of consistency, it is important to notice that for a droplet of pure water in humid air ($a_w = 1$) Eq. (1) reduces to the so-called Kelvin equation, while for a flat surface of an aqueous salt solution ($1/D \rightarrow 0$) Eq. (1) reduces to the generalized Raoult's law (Pruppacher and Klett, 2010). In this regard, estimating a_w and hence the

5   effect of the solutes dissolved in the droplet remains a challenging task, since many particles naturally present in the atmosphere and acting as CCN are formed by a mix of organic and inorganic components that exist in the same particle (Murphy et al., 1998) and have different solubility in water. Several ways to approximate a_w exist (Petters and Kreidenweis, 2007; Mason, 1971; McDonald, 1953; Kreidenweis et al., 2005; Köhler et al., 2006). In the modern parametrization of the Köhler equation proposed by (Petters and Kreidenweis, 2007), a

10   hygroscopicity parameter κ is introduced to provide a quantitative measure of the aerosol water uptake and CCN activity. This single parameter description, usually referred to as κ-Köhler theory, describes well the activity of soluble particles in a multicomponent system at thermodynamic equilibrium:

$$\frac{1}{a_w} = 1 + \kappa \frac{V_s}{V_w}, \qquad \kappa = \frac{1}{V_s} \sum_i V_{s,i} \kappa_i \qquad\qquad \text{Eq. (2)}$$

where V_s and V_w are the total volume of dry particulate matter and water, while $V_{s,i}$ and κ_i are the volume and the hygroscopicity parameter of each dry component i. The volumes are converted to their volume equivalent

15   diameter assuming spherical shape (D and d_p for solution droplets and dry particles, respectively), then a_w is introduced in Eq. (1) to yield:

$$SS(D) = \frac{D^3 - d_p^3}{D^3 - d_p^3(1 - \kappa)} \exp\left(\frac{A}{D}\right) - 1 \qquad\qquad \text{Eq. (3)}$$

$SS = SS(D)$ are usually referred to as κ-Köhler curves and calculated for different d_p as shown in Fig. 1. The maxima of the curves represent the critical supersaturation SS_c against the critical droplet diameter D_c and are of particular interest as they discriminate two very different behaviors of the nascent droplets (Pruppacher and Klett,

20   2010). The left ascending branch of the curves ($D < D_c$) represents a droplet in stable thermodynamic equilibrium: a small increase (decrease) in the size of the droplet results in the same experiencing a higher (lower) equilibrium vapor pressure that opposes the initial diameter perturbation. On the other hand, the right descending branch of the curves ($D \geq D_c$) represents unstable thermodynamic equilibrium: a small increase (decrease) in the droplet size results in the same experiencing a lower (higher) equilibrium vapor pressure, thus a

25   water droplet in this branch of the curve grows indefinitely (reduces its diameter until $D < D_c$). In this interpretation, SS_c is the minimum supersaturation required for a droplet of given diameter to grow indefinitely or, in other words, to *activate* a droplet.

Because of the functional dependence on D and of the parametric dependence on d_p and κ, Eq. (3) is difficult to use in practical cases. As all information relevant to our purposes is contained in the maxima of the κ-Köhler

30   curves, it is convenient to switch from $SS = SS(D)$ to the alternative representation $SS_c = SS_c(d_p)$. This change of coordinates is essentially possible since $SS_c = SS_c(d_p)$ is a bijective monotonic function in the range 0.05-10 µm, and it has two distinct main advantages. First, it reduces the dimensionality of the problem by removing the functional dependence $SS(D)$ that is the backbone of Eq. (3). Second, as further detailed in section

2.2, it allows introducing the equivalent functional and not merely parametric dependence $SS = SS(d_{p,c})$. This second point is particularly important since it provides a simple and direct link between the particle size distribution and the activated fraction.
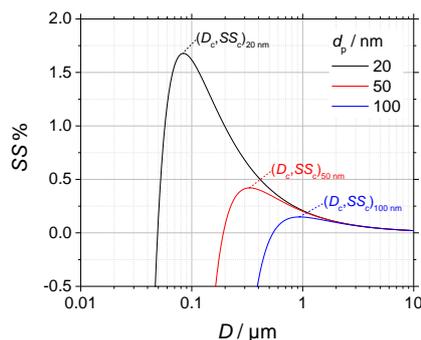
Fig. 1. Calculated κ-Kohler curves of ammonium sulfate for different dry aerosol particle diameter d_p. The maxima of the curves (critical supersaturation SS_c vs. critical droplet diameter D_c) represent the minimum conditions to activate a droplet.
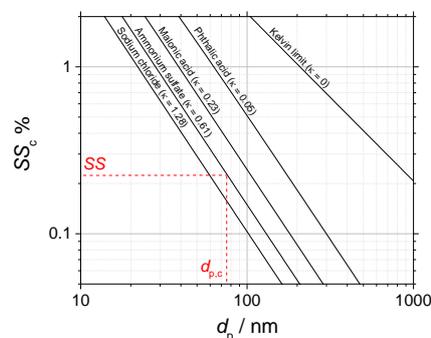
Fig. 2. Calculated $SS_c = SS_c(d_p)$ for different κ, data taken from (Petters and Kreidenweis, 2007). $d_{p,c}$ is the diameter of the smallest particles that can be activated in certain SS conditions, and it is found by projecting the environment SS on the curve of the corresponding material, and then on the d_p axis (red dashed lines).

The representation $SS_c = SS_c(d_p)$ has been widely used for the comparison of calculated and experimentally determined SS_c as a function of d_p for several single and multicomponent particles (Farmer et al., 2015; Fofie et al., 2018; Tang et al., 2016), and numerical approximations have been calculated since as early as the original implementation of κ-Köhler theory (Petters and Kreidenweis, 2007). For the sake of clarity, some examples are shown in Fig. 2: for any given value of the environment SS, the critical diameter $d_{p,c}$ is simply found by projecting SS on the curve of the corresponding component and then on the d_p axis as shown for ammonium sulfate particles. All particles having dry diameter larger than this $d_{p,c}$ are activated.

2.2. Effect of the particle distribution on the activated fraction

From a practical point of view, the activated fraction as a function of the supersaturation $F_a = F_a(SS)$ obtained from activation experiments is a convenient means to measure both SS_c and κ. F_a is defined as the ratio of the number of nucleated water droplets over the number of seeding aerosol particles:

$$F_a = \frac{N_{\text{droplets}}}{N_{\text{particles}}}$$

Eq. (4)

5   F_a can vary from zero when no activation occurs to unity when all particles/droplets are activated. Laboratory generated and naturally occurring atmospheric aerosols are polydispersed, and therefore a model taking into account their size distribution becomes important to predict the behavior of real systems. In this framework, a general relation for $F_a = F_a(d_p)$ is derived that can then be applied to specific cases. For the sake of convenience, a general aerosol size distribution function can be written as $N_T p(d_p)$, where N_T is the aerosol particles number

10   density, and $p(d_p)$ is the size probability density function normalized to unit area. According to κ-Köhler theory, at given SS all particles having diameter larger than the critical diameter $d_{p,c}$ are activated, i.e. activation has zero probability for $d_p < d_{p,c}$ and unit probability for $d_p \geq d_{p,c}$. N_{droplets} is then given by:

$$N_{\text{droplets}} = N_T \int_{d_{p,c}}^{\infty} p(d_p)\mathrm{d}d_p = N_T\left[1 - P(d_{p,c})\right]$$

Eq. (5)

where $P(x)$ is the cumulative distribution function of $p(x)$. By substituting Eq. (5) in Eq. (4) and using the normalization condition, a simple relation for F_a as a function of SS (or equivalently of $d_{p,c}$) can therefore be

15   obtained:

$$F_a(d_{p,c}) = 1 - P(d_{p,c})$$

Eq. (6)

The use of $P(d_{p,c})$ provides at the same time a simple and elegant representation of the accumulation of water droplets during activation occurring for $d_p \geq d_{p,c}$.

From this point onward, some hypotheses on the shape of the particle size distribution are required. In aerosol science, the lognormal distribution has particular interest and it is perhaps the most commonly used analytic

20   function (Heintzenberg, 1994). The probability density function $p(x)$ and the cumulative distribution function $P(x)$ of a positive random variable x whose logarithm is normally distributed are given by:

$$p(x) = \frac{1}{x\sigma\sqrt{2\pi}} e^{\frac{-(\ln x - \mu)^2}{2\sigma^2}}$$

Eq. (7)

$$P(x) = \int_{-\infty}^{x} p(t)\mathrm{d}t = \frac{1}{2} + \frac{1}{2}\mathrm{erf}\left[\frac{\ln x - \mu}{\sqrt{2}\sigma}\right]$$

Eq. (8)

where μ and σ are the mean and standard deviation of the independent variable natural logarithm, respectively. The position of the mode μ_{mode} and the geometric standard deviation σ_{geo} are given by:

$$\mu_{\text{mode}} = \exp(\mu - \sigma^2)$$

Eq. (9)

$$\sigma_{\text{geo}} = \exp(\sigma) \qquad\qquad \text{Eq. (10)}$$

By substituting Eq. (8) , Eq. (9) and Eq. (10) in Eq. (6), the activated fraction of aerosol particles having lognormal size distribution is given by:

$$F_{\text{a}}(d_{\text{p,c}}) = \frac{1}{2} - \frac{1}{2}\,\text{erf}\left[\frac{\ln d_{\text{p,c}} - (\ln \mu_{\text{mode}} + \ln^2 \sigma_{\text{geo}})}{\sqrt{2}\ln \sigma_{\text{geo}}}\right] \qquad\qquad \text{Eq. (11)}$$

For all practical intents, Eq. (11) is the master equation of this work.

3. Experimental approach

5   In this section, the methodological approach used to test the predictive capability of Eq. (11) is described. Lognormal aerosol size distribution with different μ_{mode} and σ_{geo} are compared to the experimental $F_{\text{a}} = F_{\text{a}}(SS)$ calculated using Eq. (11) for two laboratory-generated aerosols. An overview of the experimental aerosol generation setup is shown in Fig. 3(a) for ammonium sulfate, and (b) for soot. Ammonium sulfate represents the simplest case that is well known in the literature (Rose et al., 2008) for the non-aggregating, non-agglomerating,

10   quasi-spherical particles that can be generated by atomization (section 3.1). Freshly generated ammonium sulfate aerosols are size selected then injected in a 50 L Pyrex glass static reactor. From the reactor, particles are sampled for activation experiments, size and morphology measurements. The more challenging case of fractal-like soot particles is also investigated. Soot particles are generated by flame combustion, then injected in the reactor in which they undergo aging with ozone to increase κ and obtain a measurable F_{a} (section 3.2). Details on the

15   activation experiments are given in section 3.3. When necessary, all tested aerosols are selected by differential mobility analysis (DMA), and characterized using scanning mobility particle sizing (SMPS) and transmission electron microscopy (TEM) to obtain the size and morphology parameters required for calculating F_{a} (section 3.4).
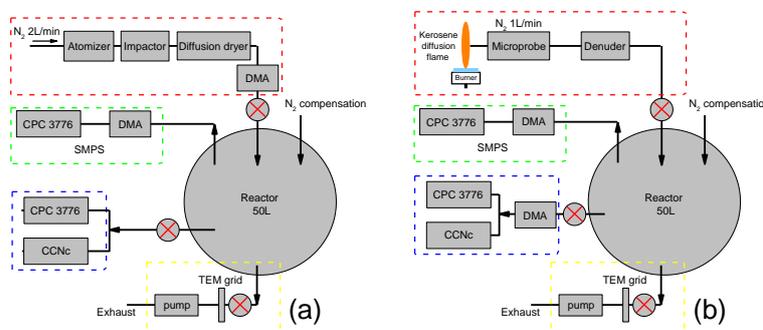
20   **Fig. 3. Overview of the experimental setup used for (a) ammonium sulfate and (b) soot. Aerosol injection system (red frame), size distribution measurement system (green frame), activated fraction measurements system (blue frame), and collection system for TEM grids (yellow frame).**

3.1. Ammonium sulfate aerosols generation

Ammonium sulfate aerosols are generated by atomization using a TSI aerosol generator 3076 loaded with 0.1 gL^{-1} concentration aqueous solution. Nitrogen is used for atomization, in the range 2-3 L min^{-1} depending on the target aerosol concentration. The excess water is removed by flowing the aerosol in a 60 cm long diffusion drier loaded with silica gel orange.

3.2. Soot aerosol generation, sampling and aging

A detailed description of the burner and sampling system is given in (Grimonprez et al., 2018). Briefly, a turbulent kerosene jet flame is stabilized on a Holthuis (previously McKenna) burner modified to allow the installation of a direct injection high efficiency nebulizer. The high speed spray of liquid fuel droplets at the exit of the nebulizer is ignited by a pilot methane flat flame on the outer ring of the modified burner, resulting in a turbulent diffusion flame of around 21 cm height. All experiments are performed using kerosene fuel Jet A-1. Soot is extracted from the jet flame at 70 and 130 mm height above the burner (HAB). At 70 mm HAB the particle concentration is small and the gas phase is rich in condensable hydrocarbons. At higher HAB, the particle concentration increases and both the diameter of the primary particles and the mobility diameter of the aggregates grow due to surface reaction and coagulation. This results in the increase of the soot volume fraction up to a peak at 130 mm HAB. Above 210 mm HAB all the particles are oxidized resulting in a non-smoking flame. Soot is sampled with a diluting quartz microprobe also detailed in (Grimonprez et al., 2018). The sampled flow is analyzed online by SMPS or deposited on Lacey grid for TEM analyses. This setup allows a fast dilution of the sampled gas up to a factor 3×10^4 that quenches most chemical reactions and limits particle coagulation and aggregation downstream in the sampling line. It is important to notice that the particle concentration in the sampling line has to be higher than the counter detection limit but low enough not to allow post-sampling aggregation or agglomeration. To avoid the formation of secondary organic aerosol in the reactors, a parallel plate, activated carbon diffusion denuder is installed downstream the microprobe.

Fresh kerosene soot particles are characterized by extremely low κ. In this work, the reaction of freshly sampled soot with ozone is used to increase κ, i.e. to lower SS_c, following the experimental procedure detailed in (Grimonprez et al., 2018). The experimental variable used to control the surface oxidation of soot particle is the so called ozone exposure, defined as the product of the ozone concentration and the residence time in the reactor. Briefly, the reactor is first pumped to reduce the background particle count below the lower detection limit of the CPC, and then is filled with nitrogen and ozone generated by photolysis of oxygen with a UVP SOG-2 lamp. To inject the soot aerosol, a slightly lower (20 mbar) pressure is set in the reactor than the sampling line. Therefore, a net sample flow (estimated around 2-5 mL min^{-1}) enters the probe from the flame, is immediately mixed with the nitrogen dilution flow (1-8 L min^{-1}), passes through the denuder and finally arrives to the reactor. The time origin for the calculation of ozone exposure starts 10 s after the end of soot injection. During injections, the SMPS is disconnected from the reactor to avoid acquiring data outside the recommended pressure range, and reconnected after the pressure has been raised again up to p = 1 bar.

3.3. Activation experiments

Activation experiments aim to measure $F_a = F_a(SS)$ and are performed by means of a commercial Droplet Measurement Technologies Cloud Condensation Nuclei counter CCNc-100 ($N_{droplets}$) installed in parallel to a TSI condensation particle counter CPC 3776 ($N_{particles}$). To study the effect of the particle size distribution on F_a, two different protocols are adopted for ammonium sulfate and soot. Ammonium sulfate particles are size selected by a DMA, pass through the reactor and then are injected in the CCNc-100. Soot particles are first sampled from the flame and injected in the reactor in which they are aged with ozone (section 3.2). A TSI differential mobility analyzer DMA 3081 is installed immediately downstream the reactor so that only aerosol particles with a selected electrical mobility and geometric deviation are injected in the CCNc-100 (Grimonprez et al., 2018). The geometric deviation is adjusted by changing the ratio between sample and sheath flow of the DMA. Additional verifications of the size distribution are performed by SMSP at regular time intervals to rule out the presence of coagulation during the aging experiments. More in detail, a 0.8 L min^{-1} particle-laden flow is sampled from the reactor, split and used to supply the CCNc (0.5 L min^{-1}) and the CPC (0.3 L min^{-1}) in parallel that record the concentration of nucleated water droplets and aerosol particles at different supersaturations, respectively, required to plot $F_a = F_a(SS)$. The total flow sampled by the CPC and the CCN is balanced with nitrogen injected directly into the reactor, and all concentrations are corrected for dilution during measurements. Samples on TEM grids are also collected to get information on the morphology and primary particle size distribution of the test aerosol. All activation experiments were taken from our previous work (Grimonprez et al., 2018).

3.4. Diagnostics

3.4.1. Aerosol particle electrical mobility and counting

SMPS measurements are performed to measure the aerosol electrical mobility diameter d_m using a TSI 3091 SMPS that consists of TSI 3080 DMA upstream a TSI 3776 CPC operated with an aerosol flow rate of 0.3 L min^{-1}. The DMA can be used independently to select aerosol particles of the desired mobility.

3.4.2. Aerosol particle morphology

TEM is used to measure the mean diameter of the primary particles D_{pp} and the number of primary particles per aggregate N_{pp} from which the fractal dimension D_f, the projection area surface A_{2D} and the maximal length of the aggregate projection L_{2D} are calculated (section 4.2). All parameters are estimated from the TEM images by using ImageJ freeware software. TEM measurements are performed on the FEI Tecnai G2 20 microscope (200 kV acceleration voltage) available at the center for electron microscopy of Lille University. All samples are deposited on Lacey carbon meshes.

4. Results and discussion

4.1. Isolated, spherical particles

To test Eq. (11), a simple case of spherical particles in the absence of aggregation and agglomeration is first considered. For hygroscopic materials having $\kappa > 0.2$, $d_{p,c}$ in Eq. (11) can be replaced by the analytic

5   approximation $d_{p,c}^3 = 4A^3/27\kappa \ln^2(1 + SS)$ (Petters and Kreidenweis, 2007). Despite its limited validity range, this approximation can be very convenient since it readily converts $F_a = F_a(d_{p,c})$ to $F_a = F_a(SS)$:

$$F_a(SS) = \frac{1}{2} - \frac{1}{2}\,\mathrm{erf}\left\{\frac{\frac{1}{3}\ln\left[\frac{4A^3}{27\kappa \ln^2(1 + SS)}\right] - \left[\ln \mu_{\mathrm{mode}} + \ln^2 \sigma_{\mathrm{geo}}\right]}{\sqrt{2}\ln \sigma_{\mathrm{geo}}}\right\} \qquad \text{Eq. (12)}$$

Eq. (12) describes the specific case of the activation of spherical, lognormally distributed hygroscopic particles ($\kappa > 0.2$). Lognormal aerosol distributions and the corresponding activation curves calculated using Eq. (12) are compared in Fig. 4 for different μ_{mode} (Fig. 4a and b), and different σ_{geo} (Fig. 4c and d). While μ_{mode} has a

10   strong impact on the position of the curve on the SS axis and a comparatively smaller effect on the slope, σ_{geo} mainly affects the shape of the activation curve. As discussed in detail in section 4.2, κ enters in all the curves as a shape parameter. A Dirac delta distribution of dry particles results in $F_a = F_a(SS)$ being a step function, with the critical supersaturation SS_c that initiates droplet nucleation being the SS at witch F_a changes value ($F_a = 1$ if $SS \geq SS_c$, $F_a = 0$ otherwise). Low σ_{geo} lognormal distributions of dry particles, typically obtained after size

15   selection during laboratory experiments and often improperly referred to as "monodisperse", result in almost symmetrical $F_a(SS)$ that do not diverge significantly from a sigmoid curve. However, high σ_{geo} lognormal distributions of dry particles, typical of naturally occurring polydispersed aerosol, result in skewed $F_a(SS)$ that can deviate significantly from the shape of a sigmoid curve. In the literature, SS_c and κ are generally retrieved by fitting $F_a = F_a(SS)$ with generic sigmoid (Grimonprez et al., 2018; Lambe et al., 2015; Sullivan et al., 2009; Tang

20   et al., 2015) or cumulative (Paramonov et al., 2013; Rose et al., 2008) functions, and SS_c is measured as $F_a(SS_c) = 0.5$. The choice of the fitting function is often a matter of convenience, and the fitting is implicitly assumed not to carry any physically meaningful parameter. However, if the dry aerosol particles do not follow a Dirac delta distribution, any fitting with a generic sigmoid curve may lead to systematic errors in the determination of SS_c.
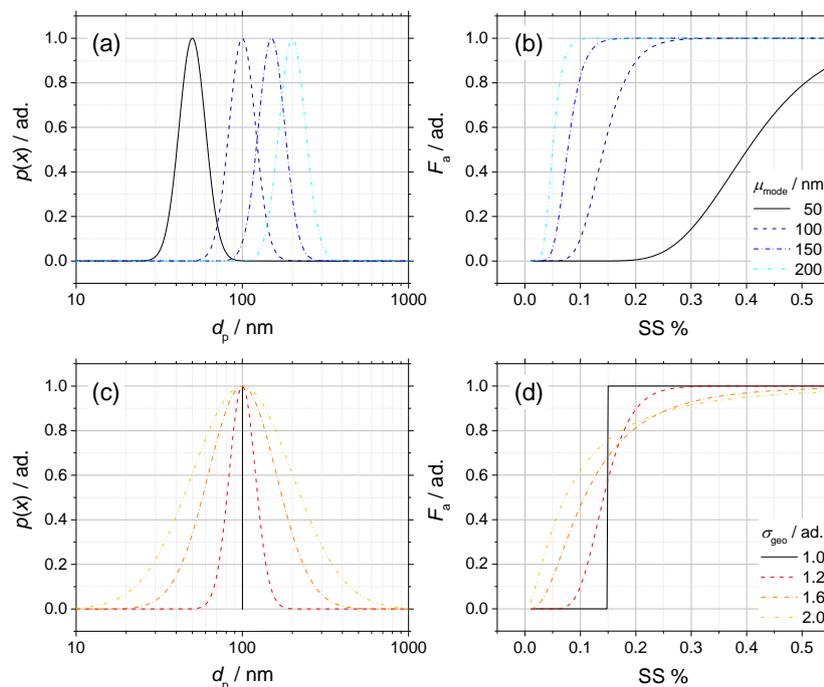
Fig. 4. (a) Normalized aerosol size distributions and (b) corresponding calculated activation curves $F_a = F_a(SS)$ calculated using Eq. (12) with $\sigma_{geo} = 1.2$ constant. (c) Normalized aerosol size distributions and (d) corresponding calculated activation curves $F_a = F_a(SS)$ calculated using Eq. (12) with $\mu_{mode} = 100$ nm constant. $\kappa = 0.61$ (ammonium sulfate) in all cases.

Ammonium sulfate is well known for the quasi-spherical particles that can be generated by atomization of its aqueous solution, and for this very reason is often used as a reference material for activation experiments (Rose et al., 2008). An example of TEM image obtained on size selected particles is shown in Fig. 5. Ammonium sulfate is hygroscopic with $\kappa = 0.61$ (Petters and Kreidenweis, 2007).
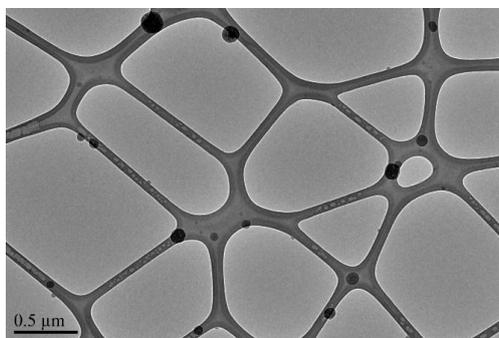
Fig. 5. TEM image of size selected ammonium sulfate aerosol (black quasi-spherical particles) deposited on a Lacey mesh, 6500 magnification.
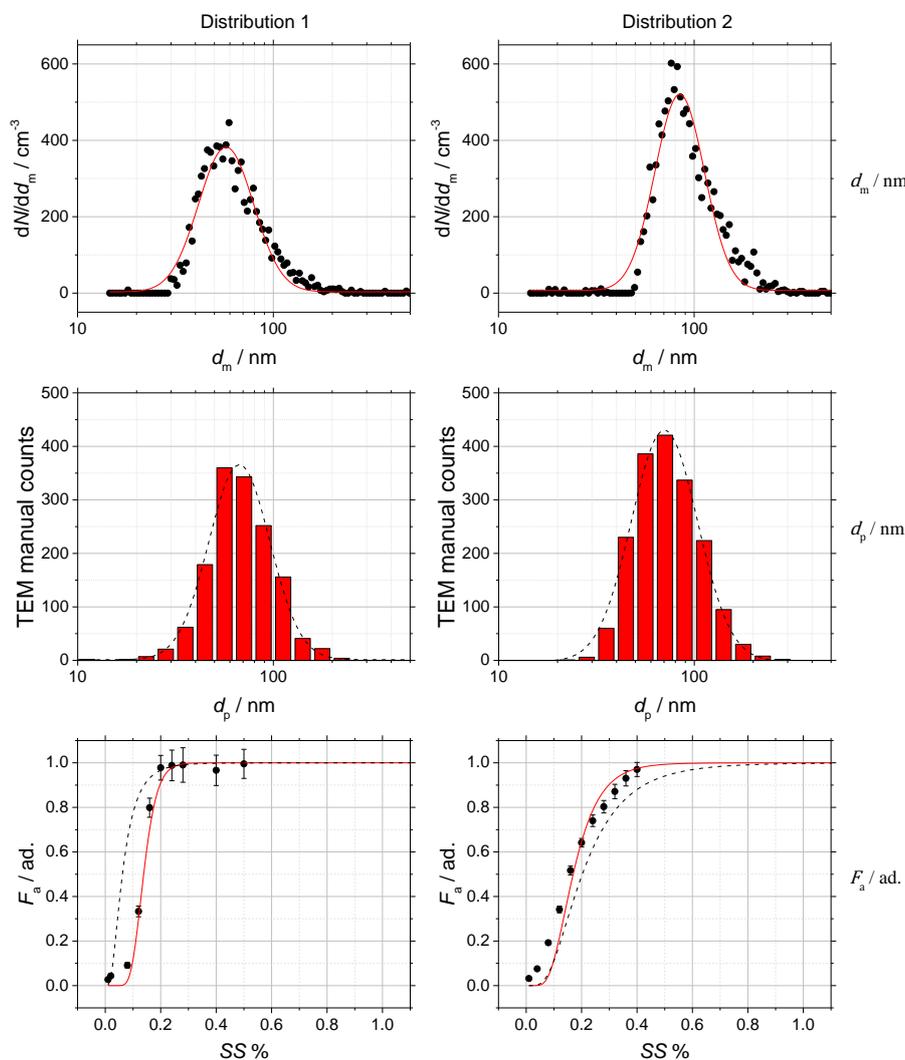
Fig. 6. Comparison of the mobility diameter d_m (black dots, top row), particle diameter d_p obtained from TEM measurements (red bars, middle row) and activated fraction F_a (black dots, bottom row) of two size distributions of ammonium sulfate nanoparticles having different μ_{mode} and σ_{geo}. The red solid lines in the left column and the black dashed lines in the middle column are the lognormal fits of d_m and d_p, respectively. The lines in the right column are F_a calculated according to Eq. (12) and using μ_{mode} and σ_{geo} obtained from measurements of d_m (red solid lines) and d_g (black dashed lines).

As shown in Fig. 6, the validity of Eq. (12) is tested with two laboratory generated ammonium sulfate aerosols by comparing $F_a = F_a(SS)$ calculated using κ, μ_{mode} and σ_{geo} as input parameters to $F_a = F_a(SS)$ obtained from activation experiments. μ_{mode} and σ_{geo} are obtained independently from electrical mobility measurements performed by SMPS (d_m, top row) and the measurement of the projected area of the particle in TEM images (d_p, middle row). The lognormal fitting functions of d_m (red solid lines) and d_p (black dashed lines) are also shown in the figure. For non-aggregating, spherical and homogeneous particles $d_m = d_p$ (Eggersdorfer and Pratsinis,

2014; Sorensen, 2011). In this work, it is found that the equivalence is true within 20% incertitude (see also Table 1). The corresponding activation data are shown in the bottom row of Fig. 6 (black filled data points) where they are compared to $F_a = F_a(SS)$ calculated according to Eq. (12) for μ_{mode} and σ_{geo} obtained from d_m (red solid lines) and from d_p (black dashed lines).

5 Globally, the activation data are in good agreement with the calculated $F_a = F_a(SS)$ as shown in the right column of Fig. 6. The mobility diameter obtained from SMPS measurements provides a much better estimation of $F_a(SS)$ than the projected area diameter obtained from TEM measurements. Some minor features of the experimental activation curves are not completely reproduced, especially the shoulder at low SS.

		Distribution 1	Distribution 2	d_m/d_p (expected: 1.0)
d_m (from SMPS)	μ_{mode} / nm	57.3±0.6	84.3±0.8	0.86
	σ_{geo} / ad.	1.38±0.04	1.34±0.04	
d_p (from TEM)	μ_{mode} / nm	67±1	70.3±0.9	1.20
	σ_{geo} / ad.	1.43±0.05	1.48±0.04	

Table 1. Electrical mobility d_m, particle diameter d_p and geometric standard deviation of the lognormal distributions of
10 **ammonium sulfate aerosol particles used in the activation experiments shown in Fig. 6. The incertitude is calculated from the lognormal fit of the distributions.**

4.2. Complex particle morphology

The predictive capability of Eq. (11) is further tested with soot aerosols. The interest in investigating soot particles as CCN herein is twofold. First, the role of the particle morphology on their activity as CCN is
15 essentially unknown, and soot particles tend to have complex fractal-like morphology that is not accounted for in the theory. Second, soot emissions are emblematic of human activities, and understanding their potential role as CCN is an important step toward understanding the anthropogenic impact on the atmosphere.

In activation experiments, soot can be generated relatively easily under controlled conditions in laboratory flames (Grimonprez et al., 2018). During the combustion process, operating on the flame conditions allows some degree
20 of control over the diameter of the primary particle and their coagulation and aggregation that in turns results on the ability of tuning the mobility diameter and morphology of the sampled aggregates. In order to apply κ-Kohler theory to soot aggregates, parametrizations that use the volume equivalent diameter d_{ve} are common (Lambe et al., 2015; Tritscher et al., 2011; Wittbom et al., 2014). In this section, we find a relationship to derive d_{ve} from the mobility diameter d_m that is the most easily accessible experimental quantity. d_{ve} is the diameter of a sphere
25 having the same volume as the aggregate, and assuming the aggregate made of identical, spherical primary particles, is defined as:

$$d_{ve} = d_{pp} N_{pp}^{\frac{1}{3}}$$

Eq. (13)

where d_{pp} and N_{pp} are the diameter and number of primary particles per aggregate, respectively. Herein, d_{pp} refers to the mode of the distribution of primary particles only, and not to the full size distribution. On the other hand, d_m is directly linked to the aerodynamic force acting on the particle (Dahneke, 1973; Tritscher et al., 2011) and can be directly obtained from SMPS measurements:

$$F_{drag} = \frac{3\pi\eta d_m v_r}{C_c(d_m)}$$ Eq. (14)

5   where η and v_r are the kinematic viscosity of the gas and the particle-gas relative velocity, and C_c is the Cunningham slip factor (Allen and Raabe, 1985):

$$C_c(K_n) = 1 + K_n\left[1.142 + 0.558\exp\left(-\frac{0.999}{K_n}\right)\right]$$ Eq. (15)

$K_n = 2\lambda_g/d_m$ is the Knudsen number and λ_g is the gas mean free path. The drag force acting on an aggregate $F_{drag,agg}$ can be approximated with the drag force acting on each primary particle $F_{drag,pp}$ which is considered as a sphere (Yon et al., 2015):

$$F_{drag,agg} = F_{drag,pp}N_{pp}^{\frac{\Gamma}{D_f}}$$ Eq. (16)

10   where D_f is the fractal dimension of the aggregate and $\Gamma = \Gamma(d_{pp})$ an exponential factor that need to be independently estimated as explained below. By introducing Eq. (14) in Eq. (16):

$$d_m = \frac{C_c(d_m)}{C_c(d_{pp})}\ d_{pp}N_{pp}^{\frac{\Gamma}{D_f}}$$ Eq. (17)

Eq. (17) is obtained by remembering that for spherical non-aggregated primary particles $d_m = d_{pp}$. The dependence on N_{pp} can be removed by using the definition of d_{ve} in Eq. (13). Finally, Eq. (17) can be solved for d_{ve} to yield:

$$d_{ve}(d_{pp}, D_f, d_m) = d_{pp}\left[\frac{d_m}{d_{pp}}\frac{C_c(d_{pp})}{C_c(d_m)}\right]^{\frac{D_f}{3\Gamma}}$$ Eq. (18)

15   d_m is easy to access from SMPS measurements, while d_{pp} and D_f can be obtained from TEM imaging as explained below.

In the variability range of the parameters tested herein, the conversion from d_m to d_{ve} does not affect the lognormal nature of the size distributions, and therefore the conversion is only applied to the modal diameter of the measured distribution at the CCN inlet, after the size selection with the DMA (see Fig. 3). The impact of the

20   conversion on the geometric standard deviation is included as a free parameter during the fitting of the activation curves.

4.2.2. d_{pp} and D_f of fractal aggregates

As mentioned above, d_{pp} and D_f are often obtained at the same time from TEM imaging, and for practical reasons this approach is followed herein as well. In this case, it is important to notice that Eq. (16) is derived for

25   the mass equivalent diameter and not for the diameter of the projected image (Yon et al., 2015). However,

whether the density of soot particles is homogeneous, the resulting d_{pp} would only be affected by a scale factor that is easily accounted for. Therefore, it is assumed that Eq. (16) can also be applied for the determination of d_{pp} from TEM imaging.
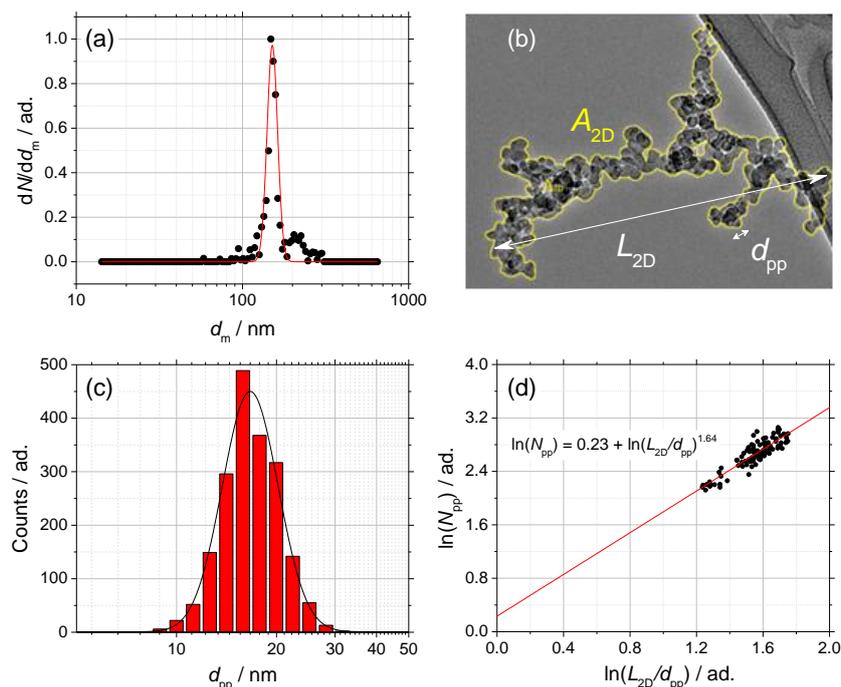
5   **Fig. 7. Soot sampled from a turbulent jet flame supplied with liquid kerosene at 130 mm HAB (Grimonprez et al., 2018) and used for the activation experiments as detailed in the text. (a) normalized mobility diameter d_m of the aggregates after size selection, μ_{mode} = 151 nm, σ_{geo} = 1.08. (b) TEM picture of a soot aggregate showing the primary particle diameter d_{pp}, the maximal length of aggregate projection L_{2D} and the projection area surface A_{2D}. (b) Primary particle size distribution and lognormal fit, mass equivalent d_{pp} = 17.7 nm, μ_{mode} = 16.7 nm and σ_{geo} = 1.21. (c) ln (N_{pp}) vs.**

10   **ln (L_{2D}/d_{pp}) plot from which the fractal dimension D_f of the soot aggregates is obtained (Eq. (20), 100 projections).**

The size distribution after DMA selection and the image of a fresh soot aggregate obtained by TEM in this work are shown in Fig. 7a and Fig. 7b, respectively. In Fig. 7b, some useful quantities are highlighted that include the primary particle diameter d_{pp}, the total surface of the aggregate in the TEM image (i.e. the projection area surface A_{2D}), and the maximal length of the aggregate projection in the TEM image (i.e. the maximal length of

15   aggregate projection L_{2D}).

Fig. 7c shows the primary particle diameter distribution of fresh soot obtained from the manual analysis of 100 TEM images (around 1900 primary particles). Although d_{pp} is often obtained from manual counting, alternative approaches exist. For instance, for a fractal aggregate, the total number of primary particle N_{pp} can also be estimated from the projection area surface A_{2D} (Köylü et al., 1995):

$$N_{pp} = k_a \left(\frac{4A_{2D}}{\pi d_{pp}^2} \right)^\alpha \qquad\qquad\qquad \text{Eq. (19)}$$

where k_a and α are the coefficient and exponent of the projection area, respectively. The values of k_a and α for soot fractal aggregates can be either calculated (Medalia, 1967) or measured (Köylü et al., 1995; Samson et al., 1987). In the past, D_f of soot aggregates has been investigated by using at least three different experimental techniques: angular light scattering (Sorensen et al., 1992), scanning electron microscopy (Colbeck et al., 1997) and of course TEM (Cai et al., 1995; Hu et al., 2003; Köylü and Faeth, 1992). In this work, we followed an approach to estimate D_f from TEM images of soot aggregates that requires measuring L_{2D} (Cai et al., 1995; Köylü et al., 1995):

$$\ln(N_{pp}) = \ln(k_g) + D_f \ln\left(\frac{L_{2D}}{d_{pp}}\right) \qquad \text{Eq. (20)}$$

Fig. 7d shows the plot $\ln(N_{pp})$ against $\ln(L_{2D}/d_{pp})$ obtained from fresh soot aggregates sampled at 130 mm HAB from the turbulent jet flame. The slope of the linear fit is $D_f = 1.64$ that is well consistent with typical values found in the literature (Cai et al., 1995; Köylü et al., 1995; Samson et al., 1987; Sorensen and Roberts, 1997; Tian et al., 2006).

4.2.3. The exponential factor Γ

Γ has been empirically estimated as a function of the Knudsen number (Yon et al., 2015) for soot particles generated with a miniCAST commercial burner (propane-air diffusion flame). In the range $1.61 < D_f < 1.79$:

$$\Gamma = 1.378 \left[\frac{1}{2} + \frac{1}{2}\operatorname{erf}\left(\frac{K_n(d_{pp}) + 4.454}{10.628}\right)\right] \qquad \text{Eq. (21)}$$

Although the variability range of D_f might seem quite restrictive, in practice it covers a region that is very representative of soot aggregates (Kelesidis et al., 2017; Yon et al., 2015). Therefore, we make an additional hypothesis that Eq. (21) can be applied to a variety of experimental investigations including our case.

4.2.4. F_a of fractal aggregates

Soot often falls in the range $\kappa < 0.2$ even after aging. Therefore, the approximation of κ-Köhler theory that leads to Eq. (12) cannot be used, and a non–analytic dependence of $d_p = d_p(SS, \kappa)$ has to be built from calculated κ-Köhler curves to obtain SS_c and remove the parametric dependence on D. Eq. (11) yields:

$$F_a(SS) = \frac{1}{2} - \frac{1}{2}\operatorname{erf}\left[\frac{\ln d_{p,c}(SS, \kappa) - \left(\ln d_{ve} + \ln^2 \sigma_{geo,ve}\right)}{\sqrt{2}\ln \sigma_{geo,ve}}\right] \qquad \text{Eq. (22)}$$

where d_{ve} and $\sigma_{geo,ve}$ replace μ_{mode} and σ_{geo}, respectively. In Eq. (22), $F_a(SS)$ shows a rather complex dependence on d_{ve}, $\sigma_{geo,ve}$ and κ, but once these parameters are known, $F_a(SS)$ is univocally defined.
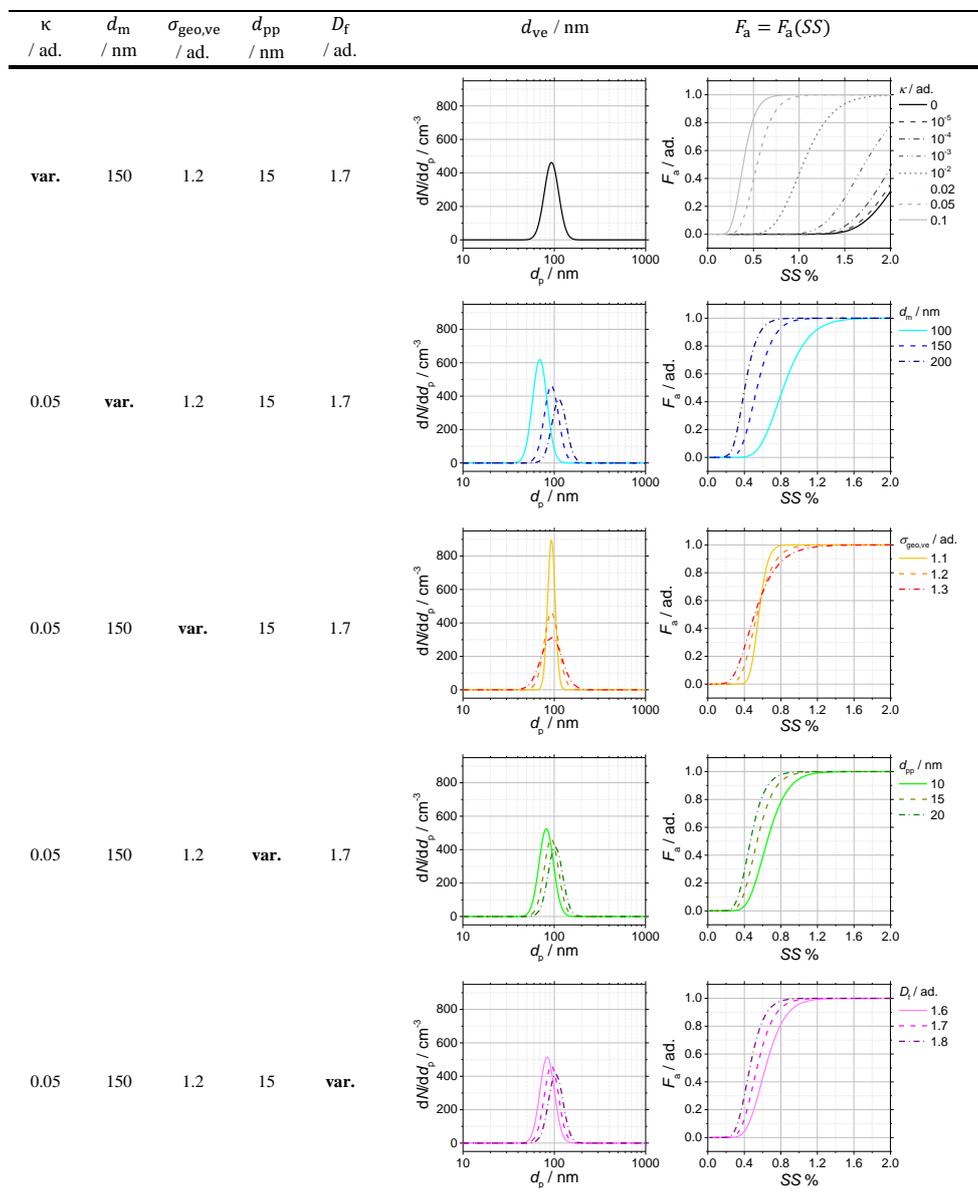
Table 2. Simulations of $F_a = F_a(SS)$ with generic aerosol particles having complex morphology as CCN according to Eq. (22). The parameters taken into account are the mobility diameter d_m, the diameter of the primary particles d_{pp}, the fractal dimension D_f, the corrected standard deviation $\sigma_{geo,ve}$ and the hygroscopicity parameter κ. The equivalent volume diameter d_{ve} is calculated from the five aforementioned variables. For each simulation, four variables are set as constant and one (marked var. in the table) is varied in the range indicated in the legend.

The functional analysis shown in Table 2 reveals that κ directly affects the shape and position of the activation curve on the SS axis, while d_m, $\sigma_{geo,ve}$, d_{pp} and D_f all have an indirect effect through d_{ve}. In particular, as noticed already in the case of isolated spherical particles, d_m impacts both the position and the slope of the activation curve, while $\sigma_{geo,ve}$ mainly affects the shape of the activation curve and especially the position of the inflection point. Similarly to the role of σ_{geo} in the case of isolated spherical particles, the smaller $\sigma_{geo,ve}$ and the

narrower the size distribution, and therefore the sharper the transition from $F_a = 0$ to $F_a = 1$. d_{pp} and D_f have a minor but still noticeable effect on d_{ve}.

$d_{ve} = d_{ve}(d_{pp}, D_f, d_m)$ can be calculated once size distribution and morphology of the aerosol are known using Eq. (18), leaving κ as the main parameter affecting the position of the activation curve on the SS axis, and in

5   turns of SS_c. Therefore, Eq. (22) can be alternatively used as a fitting function to obtain κ. If $\sigma_{geo,ve}$ cannot be directly accessed experimentally it has to be set as a free parameter to best fit the experimental data. This particular has not been estimated to be a critical issue since from the functional analysis shown in Table 2, $\sigma_{geo,ve}$ does not affect the position of the activation curve on the SS axis and therefore its effect on the determination of κ remains very limited.
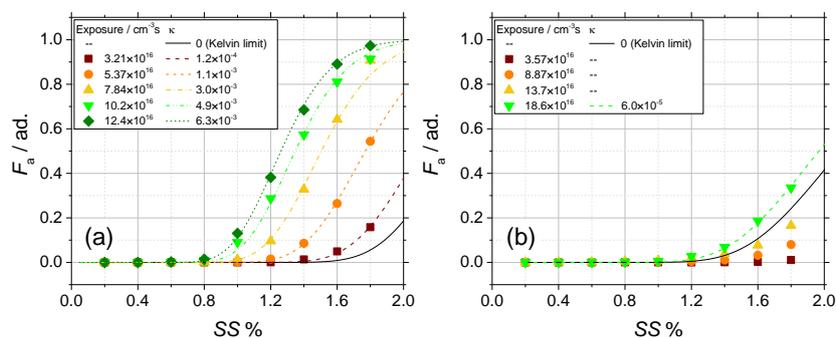
Fig. 8. Experimental (dots) and calculated (lines) activation curves of soot generated in the jet diffusion flame. (a) sampling at 70 mm HAB, d_{pp} = 13.8 nm, D_f = 1.7, $\sigma_{geo,ve}$ = 1.16, d_{ve} = 90.5 nm. (b) sampling at 130 mm HAB, d_{pp} = 16.5 nm, D_f = 1.7, $\sigma_{geo,ve}$ = 1.24, D_{ve} = 86.9 nm.

In Fig. 8, experimental (solid dots) and calculated (lines) activation curves are compared for different samples of

15   soot aerosols. These activation data are reproduced from our past investigation (Grimonprez et al., 2018). At that time, we used a simple sigmoid fitting function to determine SS_c then κ, without attributing any physical meaning to the fitting parameters. In this work, we are able to calculate $F_a = F_a(SS)$ once size and morphology of the particles are known, and only leaving κ and $\sigma_{geo,ve}$ as free parameters. In Grimonprez et al., soot is collected from the kerosene jet flame at two different HABs to show the differences in the behavior of young and reactive

20   soot (70 mm HAB) and more mature and inert soot (130 mm HAB) when exposed to ozone. Herein, d_{ve} is calculated from the mobility diameter and morphology parameters of the freshly-sampled particles that are measured by SMPS and TEM, respectively. TEM analyses before and after exposure to ozone confirm that the morphology does not change during the aging process. It is interesting to notice how the lognormal fit of the mobility diameter distribution and the calculation of the correspondent $F_a = F_a(SS)$ produce slightly different

25   geometric deviations albeit they are expected to match (σ_{geo} = 1.08, Fig. 7a, and $\sigma_{geo,ve}$ = 1.16, Fig. 8a). A possible explanation for this difference is the existence of a second mode in the mobility distribution after size selection, as shown in Fig. 7a. This second mode is much less intense than the main mode and shifted toward larger mobility diameters, and although is not accounted for by the lognormal fit, likely plays a role in the activation process.

With increasing the ozone exposure the soot particles become active at progressively lower SS. Young soot sampled at 70 mm HAB is much more reactive than mature soot sampled at 130 mm HAB, resulting in the activation curves in Fig. 8a to be shifted by a significant amount toward lower SS than the activation curves in Fig. 8b. In particular, the predictive capability of Eq. (22) is very satisfying in the case of young soot particles

5   that are efficiently converted into CCN after exposure to ozone. On the other hand, more mature soot particles show a much lower reactivity to ozone that results in the plateau of the activation curves being reached outside the dynamic range of the CCNc.

As shown in figure Fig. 8b, aging experiments of mature soot particles (130 mm HAB sampling) with exposure below $\sim 10^{15}$ cm^{-3}s produce aerosol that are only activated at very high SS. Although it is evident from Fig. 8b

10   that a weak but consistent activation occurs at high SS, this behavior is poorly reproduced by Eq. (22) and cannot be distinguished from the limit case of ideal non-interaction between water vapor and aerosol particles (Kelvin limit, $\kappa = 0$). Therefore, for all practical purposes $\kappa \sim 5 \times 10^{-5}$ has to be considered as the lowest validity limit of the model. The existence of activation data below the Kelvin limit can be a consequence of the formation of polar compounds at the soot surface from the reaction with ozone the water molecules interact with. In fact, the very

15   existence of a surface bypasses the most energy demanding steps in the formation of the first droplets, giving access to a region in the space $SS = SS(D)$ otherwise forbidden.
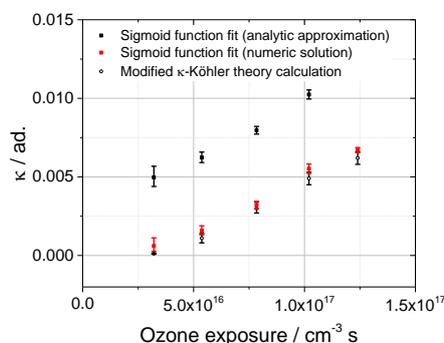
Fig. 9. κ against ozone exposure of kerosene soot sampled at 70 mm HAB, d_m = 150 nm, d_ve = 90.5 nm. The data series represent the three different approaches for the determination of κ discussed in the text: fit with Boltzmann sigmoid and

20   analytic approximation (black filled squares) or numerical calculation (red filled triangles), and from the modified κ-Köhler theory (hollow black circles). The error bars represent the incertitude on the fit, and thus are only related to κ and $\sigma_\mathrm{geo,ve}$.

The comparison of three different approaches to calculate κ from the activation data is shown in Fig. 9. In the figure, data of kerosene soot sampled at 70 mm HAB against ozone exposure are only shown. κ is calculated

25   from the fitting of the activation data with a Boltzmann sigmoid function to retrieve SS_c, and then using the analytic approximation $\kappa > 0.2$ valid for hygroscopic substances (solid black squares), or alternatively a non-approximated numerical calculation (solid red squares). The data are compared with the calculations based on Eq. (22) using $\sigma_\mathrm{geo,ve}$ as a free parameter (hollow black circles). In all cases, κ increases with ozone exposure consistently with the ongoing surface oxidation of the particles. κ obtained from the fitting with sigmoid curves

30   consistently overestimates both κ obtained from the numerical non-approximated calculation and the modified

κ-Köhler theory. In this specific case, the difference between the latter two is minimal because the dry particles are size selected before the activation experiment, and therefore the small σ_{geo} of the lognormal distribution ($\sigma_{\text{geo}} = 1.08$, see Fig. 7a) results in a symmetric activation curve very close to a sigmoid. In conclusion, once again the particle size distribution and morphology are shown to play a non negligible role on the activation of

5   aerosol particles and have to be taken into account.

The use of d_{ve} as a simple means to represent soot morphology is an important discussion point. In this work, d_{ve} is considered as representative of the activation behavior of aerosol particles, and for soot particles is calculated from the d_{m} measured at the reactor output immediately before injection in the CCNc-100. However, κ-Köhler theory is built around the idea that the soluble fraction only affects the heterogeneous nucleation of

10   droplets. The choice of the d_{ve} is justified on the basis that at some point during the soot aging process water soluble compounds form: in the κ-Köhler theory, κ parameterizes all the information on the composition of the droplet approximated as an ideal water solution. In this framework, Fig. 9 clearly shows that the chemical composition of the particles changes against the exposure time, and a likely consequence is that water soluble compounds form as products of the oxidation of the hydrocarbons adsorbed on the particle surface. This approach

15   of course does not take into account local nanoscale effects on the particle surface induced by the fractal-like morphology for instance, and some additional problems may arise (see the discussion on the Kelvin limit below for instance), and therefore future developments are possible. For instance, d_{ve} is obviously not the only diameter that can be used to parameterize the particle activation but only a very convenient one. Potentially viable alternatives include the aerodynamic or the gyration diameter for instance, however a systematic verification goes

20   well beyond the scope of this paper.

An important practical implication of this work is that size selection of the dry seeding particles before activation experiments is not mandatory as the size distribution and the geometric deviation can be taken into account in the calculation of $F_a = F_a(SS)$ to produce accurate predictions of the experimental data. In case μ_{mode} and σ_{geo} are unknown, they can be set as free parameters and the same function can alternatively be used as a fitting function.

25   This approach leads to an important simplification in the conception of activation experiments, since size selection with an SMPS system necessarily modifies the charge distribution of the dry aerosol particles, thus inevitably affecting their interaction with water molecules. Incidentally, the effect of the dry particle electrical charge on the activation is not considered in this work.

As a concluding remark, it is important to remember that Köhler theory is a classical theory entirely founded on

30   equilibrium thermodynamic, and for this very reason it is not adapted to describe phenomena occurring down to the nanoscale. The work presented herein remains a simple extension of Köhler theory that despite not requiring a detailed chemical knowledge on the CCN still manages to reproduce very well the activation behavior of isolated spherical particles without adding any ad-hoc hypothesis. Furthermore, when coupled to the empirical determination of D_{f} proposed by (Yon et al., 2015), this extension can produce rather accurate predictions of the

35   activated fraction of insoluble particles characterized by complex morphology.

5. Conclusions

Aerosol particles having complex morphology are well known to become, if certain conditions are met, important cloud condensation nuclei (CCN) in the atmosphere. The original and modern parametrization of the classical theory of nucleation are developed for spherical, isolated dry particles and droplets. In particular, the so-called

5   volume equivalent diameter d_{ve}, i.e. the diameter of a sphere having the same volume as the original particle, is often used as the dry particle diameter in κ-Köhler theory calculations. In order to investigate the activation of complex aerosols, a relation between d_{ve} used in κ-Köhler theory and the physical quantities that describe the size distribution and the morphology of aggregates is therefore necessary.

In this work, in order to make quantitative prediction on the activation curves of in the simplest case of spherical,

10   isolated dry aerosol particles, d_{ve} is approximated with the mobility diameter d_{m} and a lognormal function is directly introduced in the activation fraction function $F_{\mathrm{a}} = F_{\mathrm{a}}(SS)$. This simple model, tested with ammonium sulfate aerosols, well reproduces activation experiments and clearly shows that geometric standard deviation of the aerosol probability density function plays an important role on the shape of $F_{\mathrm{a}} = F_{\mathrm{a}}(SS)$. However, aerosols particles characterized by fractal morphology require using a more complex relation between d_{m} and d_{ve}.

15   Calculating d_{ve} of particle aggregates requires detailed knowledge of the size distribution and morphology of the particles. The approach that we propose here is based on the analysis of soot aggregate projections obtained from electron microscopy images in parallel to the measurement of their electrical mobility. In particular, the volume equivalent diameter d_{ve} is related to the primary particle diameter d_{pp}, mobility diameter d_{m} and fractal dimension D_{f} through complex and/or empirical relations. Similarly to the geometric standard deviation σ_{geo} in

20   the case of ammonium sulfate, the volume equivalent geometric standard deviation $\sigma_{\mathrm{geo,ve}}$ of soot aggregates is introduced. The effect of all morphology parameters on the activation curves are studied to provide a deeper understanding of the model. Essentially, while κ contains all information on the nature of the aerosol particle, the effect of d_{pp}, d_{m} and D_{f} are combined in d_{ve} that for all purposes of understanding activation becomes a single parameter representation of the effects of size and morphology of aggregates. On the other hand, $\sigma_{\mathrm{geo,ve}}$ plays a

25   role on the shape of the activation curves and a comparatively minor role on the determination of SS_{c}. This approach is applied to the calculation of κ of soot aged by exposure to ozone, and proved to be viable for $\kappa > 5 \times 10^{-5}$.

Data availability. The data used in this study are stored in the University of Lille servers and are available on

30   request from the corresponding author (alessandro.faccinetto@univ-lille.fr).

Author contributions. JW provided the initial version of the model. JW, SG and SB carried out the research and performed the data analysis. JW, AF, JY, PD and DP improved and refined the model. JW and AF wrote the manuscript with contributions from all authors. All authors have given approval to the final version of the

35   manuscript.

Competing interests. The authors declare that they have no conflict of interest.

Acknowledgments. This work was supported by the Agence Nationale de la Recherche through the LABEX CAPPA (ANR-11-LABX-0005), the Ministry of Higher Education and Research, Hauts-de-France Regional Council, the European Regional Development Fund (ERDF) through the Contrat de Projets Etat-Region (CPER

5   CLIMIBIO) and the MERMOSE project sponsored by the French Civil Aviation Authority (DGAC).

6. References

Allen, M. D. and Raabe, O. G.: Slip Correction Measurements of Spherical Solid Aerosol Particles in an Improved Millikan Apparatus, Aerosol Sci. Technol., 4(3), 269–286, doi:10.1080/02786828508959055, 1985.

Cai, J., Lu, N. and Sorensen, C. M.: Analysis of fractal cluster morphology parameters: structural coefficient and

10   density autocorrelation function cutoff, J. Colloid Interface Sci., 171(2), 470–473, doi:10.1006/jcis.1995.1204, 1995.

Colbeck, I., Atkinson, B. and Johar, Y.: The morphology and optical properties of soot produced by different fuels, J. Aerosol Sci., 28(5), 715–723, doi:https://doi.org/10.1016/S0021-8502(96)00466-1, 1997.

Dahneke, B. E.: Slip correction factors for nonspherical bodies - III the form of the general law, J. Aerosol Sci.,

15   4(2), 163–170, doi:10.1016/0021-8502(73)90067-0, 1973.

Eggersdorfer, M. L. and Pratsinis, S. E.: Agglomerates and aggregates of nanoparticles made in the gas phase, Adv. Powder Technol., 25(1), 71–90, doi:10.1016/j.apt.2013.10.010, 2014.

Farmer, D. K., Cappa, C. D. and Kreidenweis, S. M.: Atmospheric processes and their controlling influence on cloud condensation nuclei activity, Chem. Rev., 115(10), 4199–4217, doi:10.1021/cr5006292, 2015.

20   Fofie, E. A., Donahue, N. M. and Asa-Awuku, A.: Cloud condensation nuclei activity and droplet formation of primary and secondary organic aerosol mixtures, Aerosol Sci. Technol., 52(2), 242–251, doi:10.1080/02786826.2017.1392480, 2018.

Grimonprez, S., Faccinetto, A., Batut, S., Wu, J., Desgroux, P. and Petitprez, D.: Cloud condensation nuclei from the activation with ozone of soot particles sampled from a kerosene diffusion flame, Aerosol Sci. Technol., 52(8),

25   814–827, doi:10.1080/02786826.2018.1472367, 2018.

Heintzenberg, J.: Properties of the Log-Normal Particle Size Distribution, Aerosol Sci. Technol., 21(1), 46–48, doi:10.1080/02786829408959695, 1994.

Hu, B., Yang, B. and Köylü, Ü. Ö.: Soot measurements at the axis of an ethylene/air non-premixed turbulent jet flame, Combust. Flame, 134(1), 93–106, doi:10.1016/S0010-2180(03)00085-3, 2003.

30   Kelesidis, G. A., Goudeli, E. and Pratsinis, S. E.: Morphology and mobility diameter of carbonaceous aerosols during agglomeration and surface growth, Carbon, 121, 527–535, doi:10.1016/j.carbon.2017.06.004, 2017.

Köhler, H.: The nucleus in and the growth of hygroscopic droplets, Trans. Faraday Soc., 32(0), 1152–1161, doi:10.1039/TF9363201152, 1936.

Köhler, K. A., Kreidenweis, S. M., DeMott, P. J., Prenni, A. J., Carrico, C. M., Ervens, B. and Feingold, G.:

35   Water activity and activation diameters from hygroscopicity data - Part II: application to organic species, Atmospheric Chem. Phys., 6(3), 795–809, doi:10.5194/acp-6-795-2006, 2006.

Köylü, Ü. Ö. and Faeth, G. M.: Structure of overfire soot in buoyant turbulent diffusion flames at long residence times, Combust. Flame, 89(2), 140–156, doi:10.1016/0010-2180(92)90024-J, 1992.

Köylü, Ü. Ö., Faeth, G. M., Farias, T. L. and Carvalho, M. G.: Fractal and projected structure properties of soot aggregates, Combust. Flame, 100(4), 621–633, doi:10.1016/0010-2180(94)00147-K, 1995.

Kreidenweis, S. M., Köhler, K. A., DeMott, P. J., Prenni, A. J., Carrico, C. M. and Ervens, B.: Water activity and activation diameters from hygroscopicity data - Part I: theory and application to inorganic salts, Atmospheric Chem. Phys., 5(5), 1357–1370, doi:10.5194/acp-5-1357-2005, 2005.

Lambe, A. T., Ahern, A. T., Wright, J. P., Croasdale, D. R., Davidovits, P. and Onasch, T. B.: Oxidative aging and cloud condensation nuclei activation of laboratory combustion soot, J. Aerosol Sci., 79(Supplement C), 31–39, doi:10.1016/j.jaerosci.2014.10.001, 2015.

Mason, B.: 1971: The Physics of Clouds, Clarendon Press, Oxford., 1971.

McDonald, J. E.: Erroneous cloud physics applications of Raoult's law, J. Meteorol., 10(1), 68–70, 1953.

Medalia, A. I.: Morphology of aggregates: I. Calculation of shape and bulkiness factors; application to computer-simulated random flocs, J. Colloid Interface Sci., 24(3), 393–404, doi:https://doi.org/10.1016/0021-9797(67)90267-6, 1967.

Murphy, D. M., Thomson, D. S. and Mahoney, M. J.: In Situ Measurements of Organics, Meteoritic Material, Mercury, and Other Elements in Aerosols at 5 to 19 Kilometers, Science, 282(5394), 1664–1669, doi:10.1126/science.282.5394.1664, 1998.

Paramonov, M., Aalto, P. P., Asmi, A., Prisle, N., Kerminen, V.-M., Kulmala, M. and Petäjä, T.: The analysis of size-segregated cloud condensation nuclei counter (CCNC) data and its implications for cloud droplet activation, Atmospheric Chem. Phys., 13(20), 10285–10301, doi:10.5194/acp-13-10285-2013, 2013.

Petters, M. D. and Kreidenweis, S. M.: A single parameter representation of hygroscopic growth and cloud condensation nucleus activity, Atmospheric Chem. Phys., 7(8), 1961–1971, doi:10.5194/acp-7-1961-2007, 2007.

Pruppacher, H. R. and Klett, J. D.: Microphysics of Clouds and Precipitation, 2nd ed., Springer Netherlands. [online] Available from: https://www.springer.com/fr/book/9780792342113, 2010.

Rose, D., Gunthe, S. S., Mikhailov, E., Frank, G. P., Dusek, U., Andreae, M. O. and Pöschl, U.: Calibration and measurement uncertainties of a continuous-flow cloud condensation nuclei counter (DMT-CCNC): CCN activation of ammonium sulfate and sodium chloride aerosol particles in theory and experiment, Atmospheric Chem. Phys., 8(5), 1153–1179, doi:10.5194/acp-8-1153-2008, 2008.

Samson, R. J., Mulholland, G. W. and Gentry, J. W.: Structural analysis of soot agglomerates, Langmuir, 3(2), 272–281, doi:10.1021/la00074a022, 1987.

Sorensen, C. M.: The mobility of fractal aggregates: a review, Aerosol Sci. Technol., 45(7), 765–779, doi:10.1080/02786826.2011.560909, 2011.

Sorensen, C. M. and Roberts, G. C.: The prefactor of fractal aggregates, J. Colloid Interface Sci., 186(2), 447–452, doi:10.1006/jcis.1996.4664, 1997.

Sorensen, C. M., Cai, J. and Lu, N.: Light-scattering measurements of monomer size, monomers per aggregate, and fractal dimension for soot aggregates in flames, Appl Opt, 31(30), 6547–6557, doi:10.1364/AO.31.006547, 1992.

Sullivan, R. C., Moore, M. J. K., Petters, M. D., Kreidenweis, S. M., Roberts, G. C. and Prather, K. A.: Effect of chemical mixing state on the hygroscopicity and cloud nucleation properties of calcium mineral dust particles, Atmospheric Chem. Phys., 9(10), 3303–3316, doi:10.5194/acp-9-3303-2009, 2009.

Tang, M. J., Whitehead, J., Davidson, N. M., Pope, F. D., Alfarra, M. R., McFiggans, G. and Kalberer, M.: Cloud condensation nucleation activities of calcium carbonate and its atmospheric ageing products, Phys Chem Chem Phys, 17(48), 32194–32203, doi:10.1039/C5CP03795F, 2015.

Tang, M. J., Cziczo, D. J. and Grassian, V. H.: Interactions of water with mineral dust aerosol: water adsorption, hygroscopicity, cloud condensation, and ice nucleation, Chem. Rev., 116(7), 4205–4259, doi:10.1021/acs.chemrev.5b00529, 2016.

5   Tian, K., Thomson, K. A., Liu, F., Snelling, D. R., Smallwood, G. J. and Wang, D.: Determination of the morphology of soot aggregates using the relative optical density method for the analysis of TEM images, Combust. Flame, 144(4), 782–791, doi:10.1016/j.combustflame.2005.06.017, 2006.

Tritscher, T., Jurányi, Z., Martin, M., Chirico, R., Gysel, M., Heringa, M. F., DeCarlo, P. F., Sierau, B., Prévôt, A. S. H., Weingartner, E. and Baltensperger, U.: Changes of hygroscopicity and morphology during ageing of diesel soot, Environ. Res. Lett., 6(3), 034026, 2011.

10   Wittbom, C., Eriksson, A. C., Rissler, J., Carlsson, J. E., Roldin, P., Nordin, E. Z., Nilsson, P. T., Swietlicki, E., Pagels, J. H. and Svenningsson, B.: Cloud droplet activity changes of soot aerosol upon smog chamber ageing, Atmospheric Chem. Phys., 14(18), 9831–9854, doi:10.5194/acp-14-9831-2014, 2014.

Yon, J., Bescond, A. and Ouf, F.-X.: A simple semi-empirical model for effective density measurements of fractal aggregates, J. Aerosol Sci., 87, 28–37, doi:10.1016/j.jaerosci.2015.05.003, 2015.